

See discussions, stats, and author profiles for this publication at: <https://www.researchgate.net/publication/277004345>

Suppressing the noise in SST retrieved from satellite infrared measurements by smoothing the differential terms in regression...

Conference Paper · May 2015

DOI: 10.1111/12.2177021

CITATION

1

READS

21

3 authors, including:



B. Petrenko

National Oceanic and Atmospheric Administrat...

61 PUBLICATIONS 129 CITATIONS

[SEE PROFILE](#)



Yury Kihai

National Oceanic and Atmospheric Administrat...

46 PUBLICATIONS 150 CITATIONS

[SEE PROFILE](#)

Some of the authors of this publication are also working on these related projects:



Project

NPOESS SST improvements and Ocean Cal/Val IPO (reorganized as JPSS) [View project](#)



Project

SST Algorithm Working Group for the GOES-R program [View project](#)

Suppressing the noise in SST retrieved from satellite infrared measurements by smoothing the differential terms in regression equations

B. Petrenko^{1,2}, A. Ignatov¹ and Y. Kihai^{1,2}

¹NOAA STAR, ²GST, Inc.

ABSTRACT

Multichannel regression algorithms are widely used in retrievals of sea surface temperature (SST) from infrared brightness temperatures (BTs) observed from satellites. The SST equations typically include terms dependent on the difference between BTs observed in spectral bands with different atmospheric absorption. Such terms do account for variations in the variable atmospheric attenuation, but may introduce additional noise in the retrieved SST due to amplification of the radiometric noise. Some processing systems (e.g., the EUMETSAT OSI-SAF) incorporate noise suppression algorithms, based on spatial smoothing of the differential terms in the SST equations. A similar algorithm is being tested for the potential use in the NOAA Advanced Clear-Sky Processor for Oceans (ACSPO). The ACSPO smoothing algorithm aims to preserve natural variations in SST field, while minimizing distortions in the original SST imagery, at a minimal processing time. This presentation describes the ACSPO smoothing algorithm and results of its evaluation with the SST imagery, and with the in situ matchups for NOAA and Metop AVHRRs, Terra and Aqua MODISs, and SNPP/JPSS VIIRS.

Keywords: Sea surface temperature, algorithm, brightness temperature, regression, noise suppression

1. INTRODUCTION

Sea surface temperature (SST, T_S) is retrieved from satellite infrared observations with equations, which include terms dependent on absolute brightness temperatures (BTs) in individual bands, and on the difference ΔT_B between BTs observed in spectral bands with different atmospheric absorption, e.g., 11 μm and 12 μm ^[1-9]. The differential terms do account for variable atmospheric absorption, but they may also amplify the effect of radiometric noise on T_S ^[1,4-7]. This noise is clearly seen on small-scale SST images, and may also affect the precision of T_S as well as the performance of high-level image processing algorithms, aimed at detecting thermal fronts and SST anomalies on the ocean surface^[10].

Barton^[1] suggested suppressing the noise in the differential BT terms by averaging ΔT_B over a sliding window of 3×3 or 5×5 pixel size. This approach was implemented with SST algorithms in the EUMETSAT Ocean and Sea Ice Application Facility (OSI-SAF)^[2-4]. The concept^[1] is based on two assumptions: 1) the sensitivity of ΔT_B to SST is small; and 2) spatial scales of variations in the atmospheric absorption are much larger than those in SST. Violation of the first assumption results in smoothing spatial contrasts in T_S (equivalent to reduction in sensitivity to variations in true SST^[4]). Violation of the second assumption may introduce biases in the retrieved SST in the areas with highly variable atmospheric absorption, e.g., in the vicinity of clouds.

Several approaches were proposed to minimize these effects. In particular, Zavody et al.^[5] and then Harris and Sounders^[6] used spatial averaging of ΔT_B and then added to the retrieved T_S a term dependent on the difference between the measured and averaged BTs at 11 μm . Coll et al.^[7] replaced the mean ΔT_B with a median, which is known to better preserve regular features of the filtered field.

The spatial smoothing is now being tested in the NOAA Advanced Clear-Sky Processor for Oceans (ACSPO) used for operational SST retrievals from S-NPP VIIRS and NOAA and MetOp AVHRRs, and for experimental SST retrievals from Aqua and Terra MODIS. The baseline ACSPO SST algorithms employ^[8] the equations developed at OSI-SAF^[9]:

$$\text{Day: } T_S = a_0 + (a_1 + a_2 S_\theta) T_{11} + [a_3 + a_4 (T_S^0 - 273.15) + a_5 S_\theta] \Delta T_B + a_6 S_\theta, \quad (1)$$

$$\text{Night: } T_S = b_0 + (b_1 + b_2 S_\theta) T_{3.7} + (b_3 + b_4 S_\theta) \Delta T_B + b_5 S_\theta \quad (2)$$

Here, $T_{3.7}$, T_{11} , and T_{12} are observed BTs in bands centered at 3.7 μm , 11 μm and 12 μm , respectively; $S_\theta = \sec(\theta) - 1$; θ is the satellite view zenith angle (VZA); T_S^0 is the first guess SST (in Kelvin) obtained by interpolation of the 0.2° Canadian Meteorological Centre (CMC) L4 SST [11] to satellite pixels; a_i and b_i are regression coefficients, derived from matchups of satellite BTs with *in situ* SST, $T_{\text{in situ}}$; $\Delta T_B = T_{11} - T_{12}$. The spatial smoothing aims at separating the measured, ΔT_B , into "signal" ΔT_B^* and "noise" η :

$$\Delta T_B = \Delta T_B^* + \eta \quad (3)$$

SST with suppressed noise, T_S^* , is obtained by replacing ΔT_B with ΔT_B^* in Eq. (2) and (3):

$$\text{Day: } T_S^* = a_0 + (a_1 + a_2 S_\theta) T_{11} + [a_3 + a_4 (T_S^0 - 273.15)^0 + a_5 S_\theta] \Delta T_B^* + a_6 S_\theta, \quad (4)$$

$$\text{Night: } T_S^* = b_0 + (b_1 + b_2 S_\theta) T_{3.7} + (b_3 + b_4 S_\theta) \Delta T_B^* + b_5 S_\theta. \quad (5)$$

The following features of the ACSPO smoothing algorithm should be noted:

First, since the difference in ΔT_B at neighboring clear-sky and cloudy pixels can be large, mixing clear-sky and cloudy pixels during spatial averaging may cause significant biases between T_S^* and T_S . Customarily, cloudy pixels are screened out with the cloud mask before the SST retrieval. In ACSPO, however, SST is first retrieved over all ocean pixels, before the ACSPO Clear-Sky Mask (ACSM) is generated [12]. This allows using SST as an important cloud predictor but precludes screening cloudy pixels during spatial smoothing. Therefore, the smoothing algorithm in ACSPO detects the presence of both clear and cloudy pixels within the sliding window by elevated spatial variations in ΔT_B .

Second, the smoothing of spatial contrasts in T_S^* is minimized in ACSPO by estimating ΔT_B^* from a local regression between ΔT_B and T_{11} , rather than by simple averaging of ΔT_B . This way, a component of ΔT_B correlated with T_{11} is explicitly determined and preserved. Another reason for choosing this approach (rather than, e.g., the median-based approach [7]) is that all required statistics can be calculated with fast algorithms suitable for parallel computations.

The performance of the ACSPO SST algorithm with smoothing the BT differential term is demonstrated in Section 2. The estimates of the suppressed SST noise are provided in Section 3.

2. SPATIAL SMOOTHING IN ACSPO

The performance of the ACSPO smoothing algorithm is demonstrated here on a daytime scene observed by MetOp-A AVHRR over the Atlantic Ocean off the Southern American coast on 31 January 2015. Fig. 1a and 1b demonstrate the images of T_{11} and ΔT_B . Cloudy pixels detected with the ACSM are rendered in gray. Similar large-scale features in Fig. 1a and 1b suggest substantial correlation between T_{11} and ΔT_B . The fine temperature scale in Fig. 1b was specifically selected to emphasize the noise in ΔT_B . However, the image of retrieved T_S in Fig. 1c, which uses a much larger scale, also shows elevated noise in some areas. The noise in T_S is even more noticeable in Fig. 1d, which shows deviations of T_S from the first guess CMC L4 SST, T_S^0 .

The simplest way to obtain ΔT_B^* is to average ΔT_B over all pixels within a certain sliding window:

$$\Delta T_B^* = \langle \Delta T_B \rangle. \quad (6)$$

Here, $\langle \cdot \rangle$ denotes averaging over the sliding window. Fig. 2 demonstrates the images of the suppressed component in ΔT_B , $\eta = \Delta T_B - \Delta T_B^*$, and in T_S , $\mu = T_S - T_S^*$ for a case of 11×11 sliding window. Along with random components, both images include regular features such as fringes of systematically cold pixels near cloud, caused by mixed "clear" and "cloudy" pixels, and stripes collocated with large T_{11} and T_S gradients (cf. Fig. 1a,c). Substituting ΔT_B^* defined by (6) into Eq. (4) thus leads to two artifacts: it systematically warms up T_S^* near clouds and smoothes large SST gradients in the clear-sky areas.

These artifacts can be reduced by analysis of spatial statistics of ΔT_B and T_{11} within the sliding window. Fig. 3a demonstrates the image of spatial standard deviation (SD) of ΔT_B , $\sigma(\Delta T_B)$, averaged within 11×11 sliding windows over

all pixels, including both “clear” and “cloudy”. In the most uniform regions $\sigma(\Delta T_B)$ does not exceed ~ 0.1 K, but increases in the neighborhood of large T_S gradients (cf. Fig. 1c) and may exceed 0.2 K in the vicinity of clouds. This suggests that $\sigma(\Delta T_B)$ may be used as an indicator of mixing clear and cloudy pixels within a sliding window. Fig. 3b shows the image of spatial correlation coefficient between T_{II} and ΔT_B , $C(T_{II}, \Delta T_B)$. The correlation is small in relatively uniform areas but becomes significantly positive or negative in the areas of large T_S gradients and near clouds. From physical considerations, elevated positive values of $C(T_{II}, \Delta T_B)$ can be attributed to areas with high SST gradients and nearly constant atmospheric absorption, whereas increased negative values of $C(T_{II}, \Delta T_B)$ may indicate areas of variable atmospheric absorption near clouds. Comparison of Fig. 3a with the image of SD of T_{II} , $\sigma(T_{II})$ in Fig. 3c suggests that larger values of $\sigma(\Delta T_B)$ are usually associated with larger values of $\sigma(T_{II})$.

Significant values of $C(T_{II}, \Delta T_B)$ in the areas with larger $\sigma(\Delta T_B)$ and $\sigma(T_{II})$ suggest that the estimate (6) of ΔT_B^* can be improved by establishing local regressions between ΔT_B and T_{II} :

$$\Delta T_B^* = \langle \Delta T_B \rangle \quad \text{if } \sigma(T_{II})=0 \quad (7a)$$

$$\Delta T_B^* = \langle \Delta T_B \rangle + [C(T_{II}, \Delta T_B) \sigma(\Delta T_B) / \sigma(T_{II})] (T_{II} - \langle T_{II} \rangle) \quad \text{if } \sigma(T_{II})>0 \quad (7b)$$

Fig. 3d shows residual SD for the estimate (7), $\sigma_{res}(\Delta T_B)$ estimated as follows:

$$\sigma_{res}(\Delta T_B) = \sigma(\Delta T_B) \quad \text{if } \sigma(T_{II})=0 \quad (8a)$$

$$\sigma_{res}(\Delta T_B) = \sigma(\Delta T_B) [1 - C(T_{II}, \Delta T_B)^2] \quad \text{if } \sigma(T_{II})>0 \quad (8b)$$

Note that $\sigma_{res}(\Delta T_B)$ never exceeds $\sigma(\Delta T_B)$. Comparison of Fig. 3d with Fig. 3a demonstrates that, unlike $\sigma(\Delta T_B)$, $\sigma_{res}(\Delta T_B)$ is not increasing in the areas of large SST gradients because the estimate (7b) better accounts for regular variations in ΔT_B than the estimate (6). However, $\sigma_{res}(\Delta T_B)$ remains large in the narrow area around clouds in Fig. 3d. In order to avoid systematic bias in ΔT and T_{II} in this area, we modify Eq. (7) by posing an upper limit, σ_{max} , on the values of $\sigma(\Delta T_B)$ and $\sigma_{res}(\Delta T_B)$ at which the spatial averaging is performed:

$$\Delta T_B^* = \Delta T_B \quad \text{if } (\sigma(T_{II})=0 \text{ and } \sigma(\Delta T_B)>\sigma_{max}) \text{ or } (\sigma(T_{II})>0 \text{ and } \sigma_{res}(\Delta T_B)>\sigma_{max}) \quad (9a)$$

$$\Delta T_B^* = \langle \Delta T_B \rangle \quad \text{if } \sigma(T_{II})=0 \text{ and } \sigma(\Delta T_B)<\sigma_{max} \quad (9b)$$

$$\Delta T_B^* = \langle \Delta T_B \rangle + [C(T_{II}, \Delta T) \sigma(\Delta T) / \sigma(T_{II})] (T_{II} - \langle T_{II} \rangle) \quad \text{if } \sigma(T_{II})>0 \text{ and } \sigma_{res}(\Delta T_B)<\sigma_{max} \quad (9c)$$

Fig 4 demonstrates the suppressed components in ΔT_B , $\eta = \Delta T_B - \Delta T_B^*$, and in T_S , $\mu = T_S - T_S^*$, for the case when ΔT_B^* is estimated from Eq. (9), with 11×11 sliding window $\sigma_{max}=0.15$ K. The regular components in Fig. 4 are strongly reduced compared with Fig. 2, with values of ΔT_B^* biased cold near clouds replaced with the initial ΔT_B values.

The last step of the smoothing algorithm is processing of those pixels left unprocessed by the algorithm (9a-c), with the same algorithm but using the minimal possible sliding window of 3×3 pixels. The reduction in the window size may make the estimates of the statistics in (9) less reliable, but allows extending smoothing to the pixels in the closest neighborhood of clouds. Fig. 5 shows that the stripes of unprocessed pixels around clouds practically disappear in the final images produced with the full smoothing algorithm, using sliding windows of 11×11 and 3×3 sequentially.

Fig. 6 shows results of SST retrieval with the algorithm (3), using two sizes of sliding window as described above (cf. Fig. 1c and d, which shows the images of T_S and $T_S - T_S^0$ for the regular Eq. (1) without spatial smoothing. Note that the difference between SSTs presented in Fig. 1c and Fig. 6a is shown in Fig. 5b. Fig. 6 confirms that the ACSPO smoothing algorithm suppresses a large part of the noise in retrieved SST without significant modification of regular components in T_S . The power of the suppressed noise in retrieved SST is quantified in Section 3.

3. THE EFFECT OF SPATIAL SMOOTHING ON PRECISION OF RETRIEVED SST

The ACSPO smoothing algorithm has two parameters: the size of the larger sliding window D_1 and the maximum SD of clear-sky variations in ΔT_B within the sliding window, σ_{max} . The size of the smaller sliding window, D_2 , is always set to the minimum possible value, $D_2=3$. D_1 and σ_{max} were selected for all AVHRR (GAC and FRAC), MODIS and VIIRS

sensors by establishing a visual tradeoff between the random noise and regular detail in the images of suppressed components of ΔT_B and T_S . Table 1 lists the values of D_1 and σ_{max} adopted in ACSPO testing.

Table 1. Parameters of the smoothing algorithm for different satellite sensors

Parameter	VIIRS	MODIS Aqua and Terra	AVHRR FRAC	AVHRR GAC
D_1	11	11	11	7
σ_{max}	0.05 K	0.05 K	0.15 K	0.12 K

To evaluate the effect of spatial smoothing on SD of retrieved minus *in situ* SST, the matchup data sets (MDS) were collected from 6 January 2015 – 18 February 2015 for six satellite sensors, including the S-NPP VIIRS, Aqua and Terra MODIS, MetOp-A and Metop-B AVHRR (FRAC), and NOAA19 AVHRR (GAC). Data of each sensor were processed with ACSPO. Clear-sky BTs were selected with ACSM [12] and matched with quality controlled *in situ* SSTs from the *in situ* Quality Monitor (*iQuam* [13], available at www.star.nesdis.noaa.gov/sod/sst/iquam/). Table 2 presents global biases and SDs of SSTs with respect to *in situ* SST averaged over the full MDS, retrieved without and with spatial smoothing, separately for day and night. Table 2 also shows the RMS level of suppressed noise σ_N estimated as

$$\sigma_N = [\sigma(T_S)^2 - \sigma(T_S^*)^2]^{1/2} \quad (10)$$

Here, $\sigma(T_S)$ and $\sigma(T_S^*)$ are SDs of SSTs retrieved with (T_S) and without (T_S^*) spatial averaging, with respect to *in situ* SST.

Table 2. Bias and SD (both in degrees Kelvin) of T_S to T_S^* and RMS levels of suppressed noise estimated from matchups with *in situ* SSTs, for six satellite sensors, for day and night.

Algorithm	Statistics	VIIRS	AQUA	TERRA	Metop-A	Metop-B	NOAA19
Day							
Without smoothing	Bias	0.000	0.068	0.057	0.023	-0.013	-0.005
	SD	0.371	0.416	0.424	0.401	0.405	0.454
With smoothing	Bias	-0.002	0.064	0.053	0.010	-0.008	-0.005
	SD	0.368	0.409	0.415	0.382	0.389	0.449
	RMS noise	0.05	0.08	0.09	0.12	0.11	0.07
Night							
Without smoothing	Bias	-0.012	0.029	0.052	0.011	-0.032	-0.008
	SD	0.289	0.318	0.311	0.327	0.316	0.392
With smoothing	Bias	0.012	0.029	0.050	0.006	-0.028	-0.007
	SD	0.288	0.317	0.309	0.326	0.315	0.391
	RMS noise	0.02	0.03	0.045	0.03	0.03	0.03

In all cases, the spatial smoothing does reduce SDs of fitting *in situ* SST. The absolute reduction is from 0.003 K to 0.019 K during the daytime and from 0.001 K to 0.002 K at night. This seemingly small effect, however, corresponds to more significant RMS levels of suppressed noise, ranging from 0.05 K to 0.12 K for daytime and from 0.02 to 0.045 K for nighttime data. Table 3 demonstrates similar statistics, but estimated with respect to CMC over all clear-sky pixels detected during processing satellite observations for 31 January 2015.

As in Table 2, the SDs of T_S^* minus CMC are in all cases consistently smaller than corresponding SDs for the case without smoothing. The estimated RMS suppressed noise in Table 3 is comparable with the corresponding statistics with respect to *in situ* SST in Table 2.

The weights of the differential terms in Eq. (1,2) and Eq. (3,4) are the functions of VZA and, during the daytime, of the first guess SST, T_S^θ . This suggests the dependency of the RMS suppressed noise in T_S from these variables. Since T_S^θ almost monotonically changes with latitude, the daytime dependency of the T_S noise from latitude is also significant. Fig. 7 demonstrates σ_N , estimated with respect to CMC from observations made with six satellite sensors during night and

day on 31 January 2015. The maximum of the SST noise takes place in the low latitudes. The maximum RMS SST noise of ~ 0.15 K is observed for daytime MetOp-A AVHRR, and VIIRS provides the lowest level of the RMS SST noise. At night, the RMS SST noise is nearly flat as a function of latitude.

Table 3. Same as in Table 2 but with respect to CMC L4 SST.

Algorithm	Statistics	VIIRS	AQUA	TERRA	Metop-A	Metop-B	NOAA19
Day							
Without smoothing	Bias	0.283	0.288	0.119	0.019	-0.032	0.286
	SD	0.526	0.523	0.436	0.407	0.411	0.548
With smoothing	Bias	0.282	0.285	0.117	0.013	-0.032	0.286
	SD	0.522	0.515	0.421	0.382	0.392	0.538
RMS noise		0.07	0.09	0.11	0.14	0.12	0.10
Night							
Without smoothing	Bias	0.035	0.041	0.102	0.093	0.036	0.007
	SD	0.315	0.335	0.332	0.345	0.337	0.364
With smoothing	Bias	0.035	0.040	0.102	0.092	0.036	0.008
	SD	0.314	0.333	0.330	0.342	0.334	0.362
RMS noise		0.03	0.04	0.04	0.05	0.04	0.04

Fig. 8 demonstrates the dependencies of RMS suppressed noise in SST on VZA, for night and day. In all cases, σ_N increases with VZA, especially for the daytime.

SUMMARY

The ACSPO algorithm for smoothing the BT difference in the regression SST equations estimates the smoothed value from regression between the BT difference and the leading BT (T_{11} during the daytime and $T_{3.7}$ at night), within a sliding window surrounding a given pixel, rather than with an average over the sliding window. This improves the separation of random noise from regular features and preserves original magnitudes and sharpness of spatial SST contrasts. The algorithm does not require an external cloud mask. The presence of both “clear” and “cloudy” pixels within the sliding window is detected by elevated SD of the BT difference. Once such situation has been detected, the size of the sliding window is reduced to 3×3 pixel, to minimize the number of unprocessed pixels near clouds. The algorithm requires calculating local statistics of ΔT_B and T_{11} (or $T_{3.7}$), such as means, SDs and correlation coefficient, for all ocean pixels. This is accomplished within ACSPO with fast algorithms using parallel processing. Full processing of a 10 minutes ACSPO VIIRS granule, for instance, takes ~ 1 min, of which the smoothing itself takes less than 1 sec.

ACKNOWLEDGMENTS

This work was conducted under the JPSS and Geostationary Operational Environmental Satellite-R Series (GOES-R) Projects funded by the corresponding Program Offices. We thank JPSS Program Scientist Mitch Goldberg and AWG Manager Jaime Daniels. Thanks also go to our NOAA colleagues John Sapper, John Stroup, Prasanjit Dash, XingMing Liang and Feng Xu for assistance, discussions, and feedback at its different stages. The views, opinions, and findings contained in this paper are those of the authors and should not be construed as an official NOAA or US Government position, policy, or decision.

REFERENCES

- [1] Barton, I.J., “Digitization effects in AVHRR and MCSST data,” *Remote Sens. Environ.*, **29**, 87-89 (1989), [http://dx.doi.org/10.1016/0034-4257\(89\)90081-3](http://dx.doi.org/10.1016/0034-4257(89)90081-3).
- [2] Brisson, A., Le Borgne, P. and Marsuin, A., “Results of one year of preoperational production of sea surface temperature from GOES-8,” *J. Atmos. Oceanic Technol.*, **19**, 1638-1652 (2002), [http://dx.doi.org/10.1175/1520-0426\(2002\)019%3C1638:ROOYOP%3E2.0.CO;2](http://dx.doi.org/10.1175/1520-0426(2002)019%3C1638:ROOYOP%3E2.0.CO;2)

- [3] Le Borgne, P., “OSI-SAF Low Earth Orbiter Sea Surface Temperature Product User Manual,” Version 2.1. The EUMETSAT Network of Satellite Application Facilities, OSI-SAF (2009), http://www.osi-saf.org/biblio/docs/ss1_pum_leo_sst_2_1.pdf
- [4] Merchant. C. J., Le Borgne, P., Roquet H., and Legendre, G., “Extended optimal estimation techniques for sea surface temperature from the Spinning Enhanced Visible and Infra-Red Imager,” *Remote. Sens. Environ.*, **131**, 287-297 (2013), <http://dx.doi.org/10.1016/j.rse.2012.12.019>, .
- [5] Zavody, A.M., Mutlow C.T. and Llewellyn-Jones, D., “A radiative transfer model for sea surface temperature retrieval for the along-track scanning radiometer,” *J. Geophys. Res.*, **100**, 937-952 (1995), doi: 10.1029/94JC02170
- [6] Harris, A.R. and Sounders, M.A., “Global validation of the along-track scanning radiometer against drifting buoys,” *J. Geophys. Res.*, **101**, 12127-12140 (1996), doi: 10.1029/96JC00317.
- [7] Coll, C., Caselles V. and Valor, E., “Atmospheric correction and determination of sea surface temperature in midlatitudes from NOAA-AVHRR data,” *Atmos. Research*, **30**, 233-250 (1993), [http://dx.doi.org/10.1016/0169-8095\(93\)90026-K](http://dx.doi.org/10.1016/0169-8095(93)90026-K).
- [8] Petrenko, B., Ignatov, A., Kihai, Y., Stroup, J. and Dash, P., “Evaluation and selection of SST regression algorithms for JPSS VIIRS,” *J. Geophys. Res.*, **119**, 4580–4599 (2014), doi:[10.1002/2013JD020637](https://doi.org/10.1002/2013JD020637).
- [9] Lavanant, L., Le Borgne, P., Legendre, G., Marsouin, A., Pere, S. and Roquet, H. (2012), “VIIRS SST at OSI-SAF,” GHRSSST XIII Science Team Meeting, Tokyo, Japan, p.235, <https://www.ghrsst.org/documents/q/category/ghrsst-science-team-meetings/ghrsst-xiii-tokyo-japan/proceedings/>.
- [10] Gladkova I., Kihai, Y., Ignatov, A., Shahriar, F., and Petrenko, B., “SST pattern test in ACSPO clear-sky mask for VIIRS,” *Remote. Sens. Environ.*, **160**, 87-98 (2015), <http://dx.doi.org/10.1016/j.rse.2015.01.003>
- [11] Brasnett, B. “The impact of satellite retrievals in a global SST analysis,” *Q. J. R. Meteorol. Soc.*, **134**, 1745-1760 (2008), doi: 10.1002/qj.319.
- [12] Petrenko, B., Ignatov, A., Kihai, Y. and Heidinger, A., “Clear-sky mask for the Advanced Clear-Sky Processor for Oceans,” *J. Atmos. Oceanic Technol.*, **27**, 1609–1623 (2010), <http://dx.doi.org/10.1175/2010JTECHA1413.1>.
- [13] Xu, F. and Ignatov A., “In situ SST Quality Monitor (*iQuam*),” *J. Atmos. Oceanic Technol.*, **31**, 164-180 (2014), doi: <http://dx.doi.org/10.1175/JTECH-D-13-00121.1>

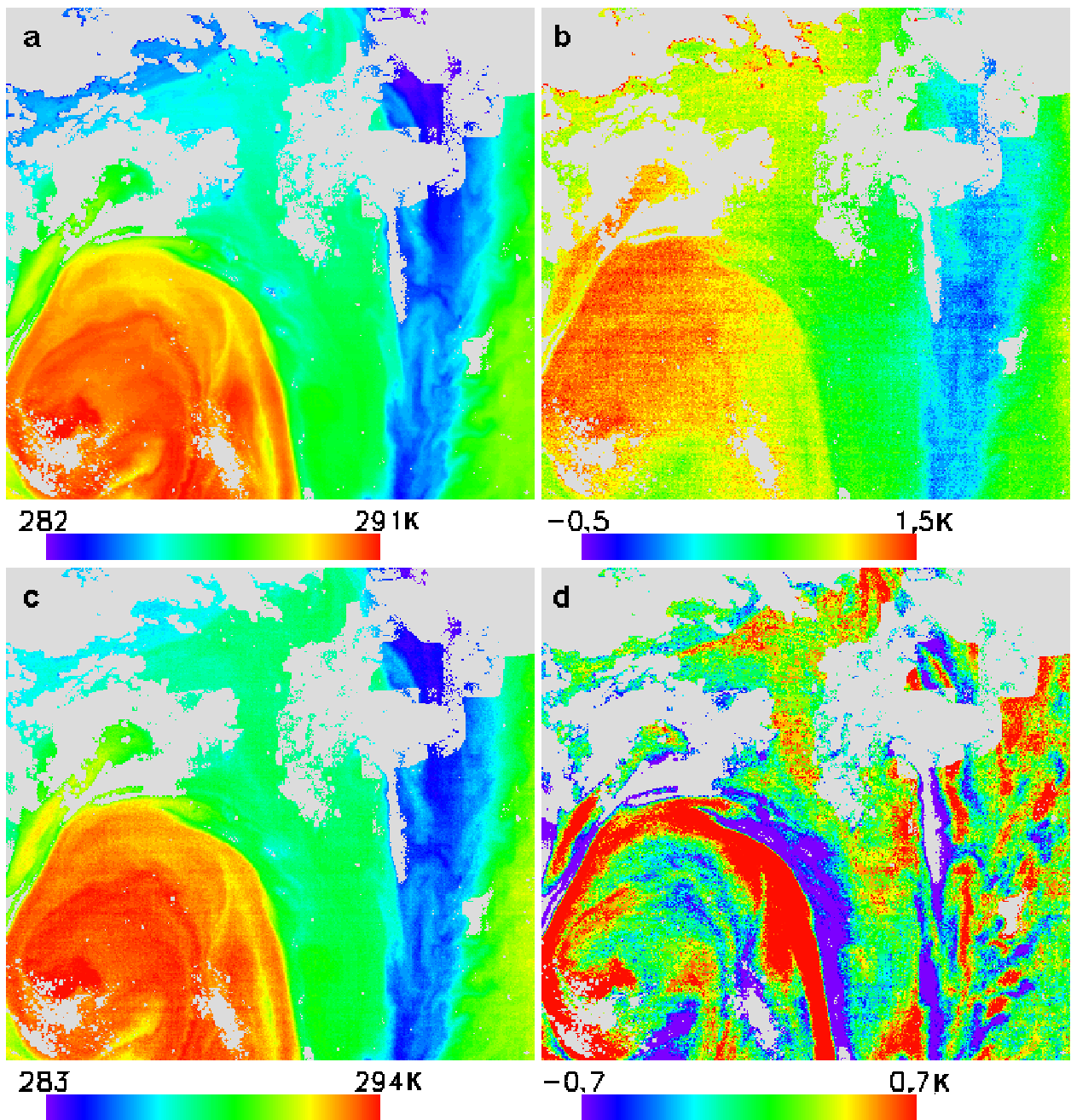


Fig.1. The images of (a) T_{II} , (b) ΔT_{II-I2} , (c) T_S and (d) $T_S - T_S^0$ produced from daytime MetOp-A observations over the Southern Atlantic on 31 January 2015.

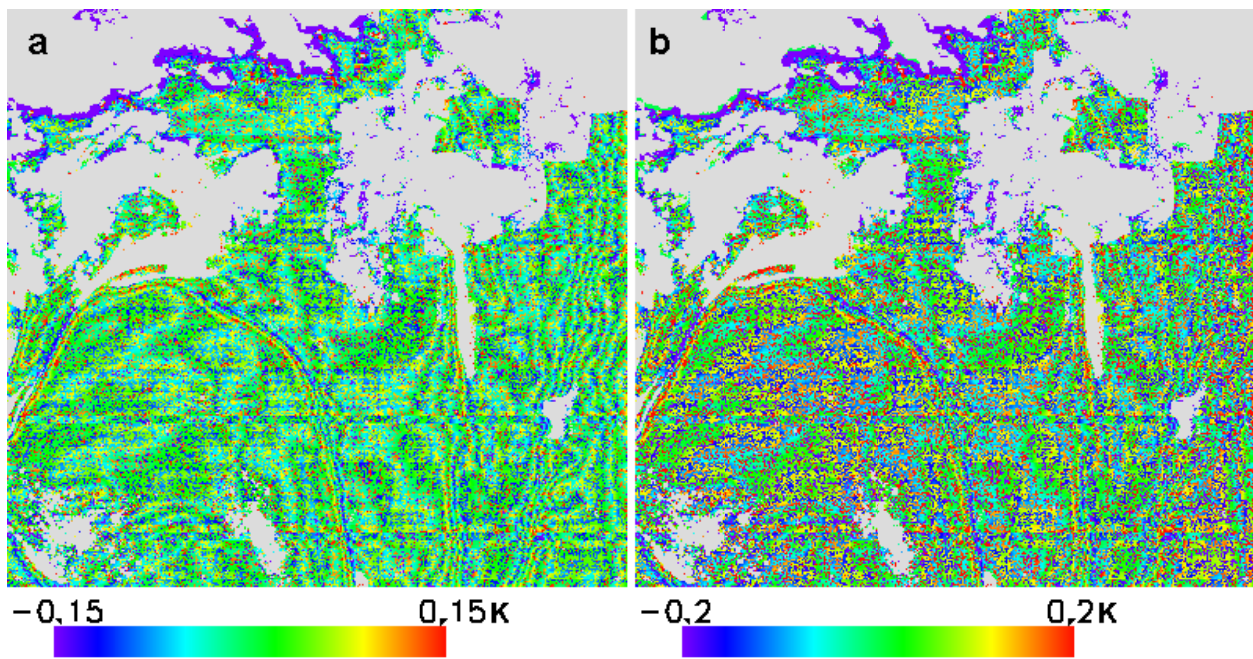


Fig. 2. The images of suppressed components in (a) ΔT_B and (b) T_S for the case when ΔT_B^* is obtained from averaging all pixels within 11×11 sliding window.

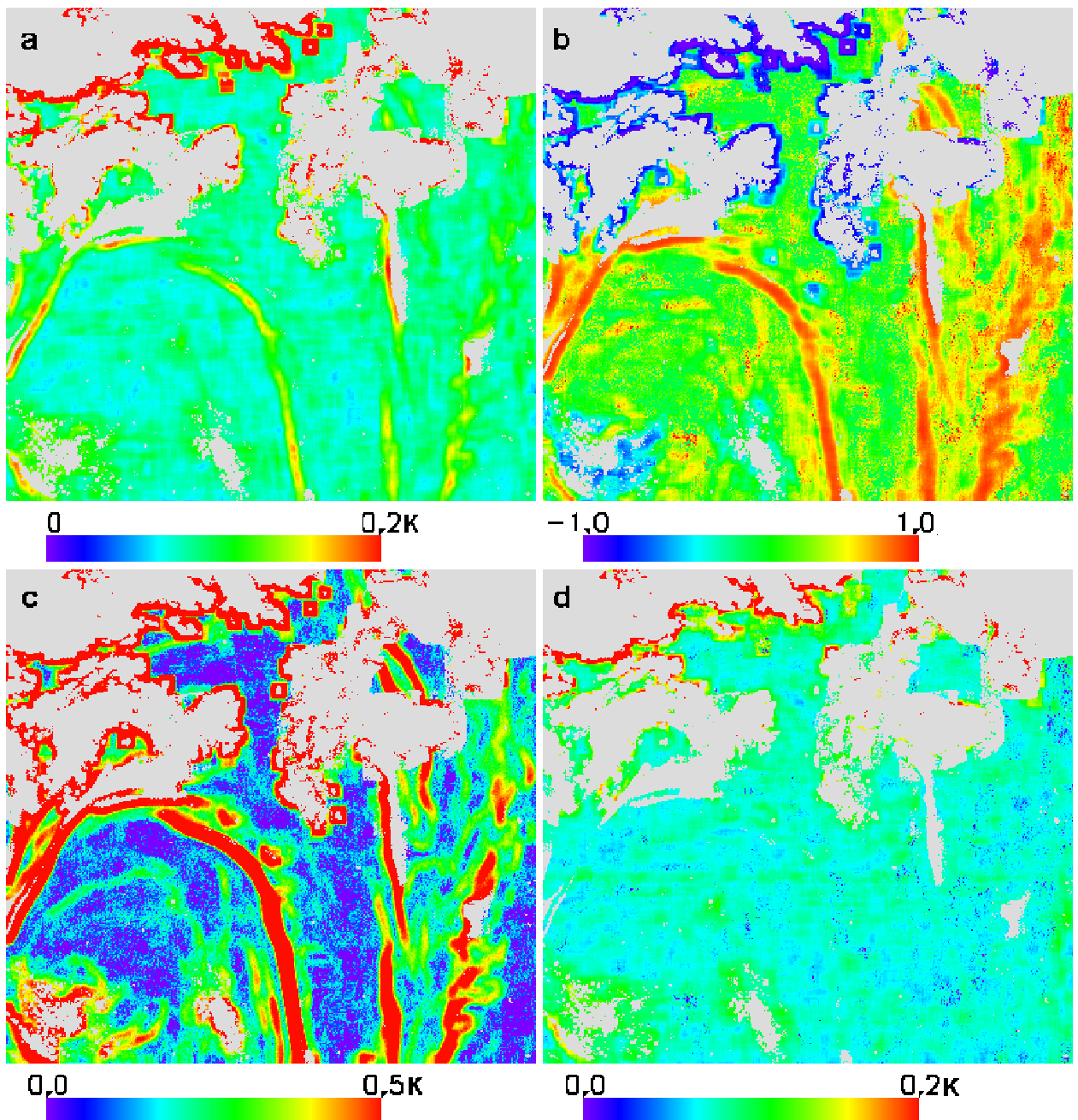


Fig. 3. The images of (a) SD of ΔT_B , (b) correlation between ΔT_B and T_{II} , (c) SD of T_{II} and (d) residual SD of regression estimate of ΔT_B within 11×11 sliding windows.

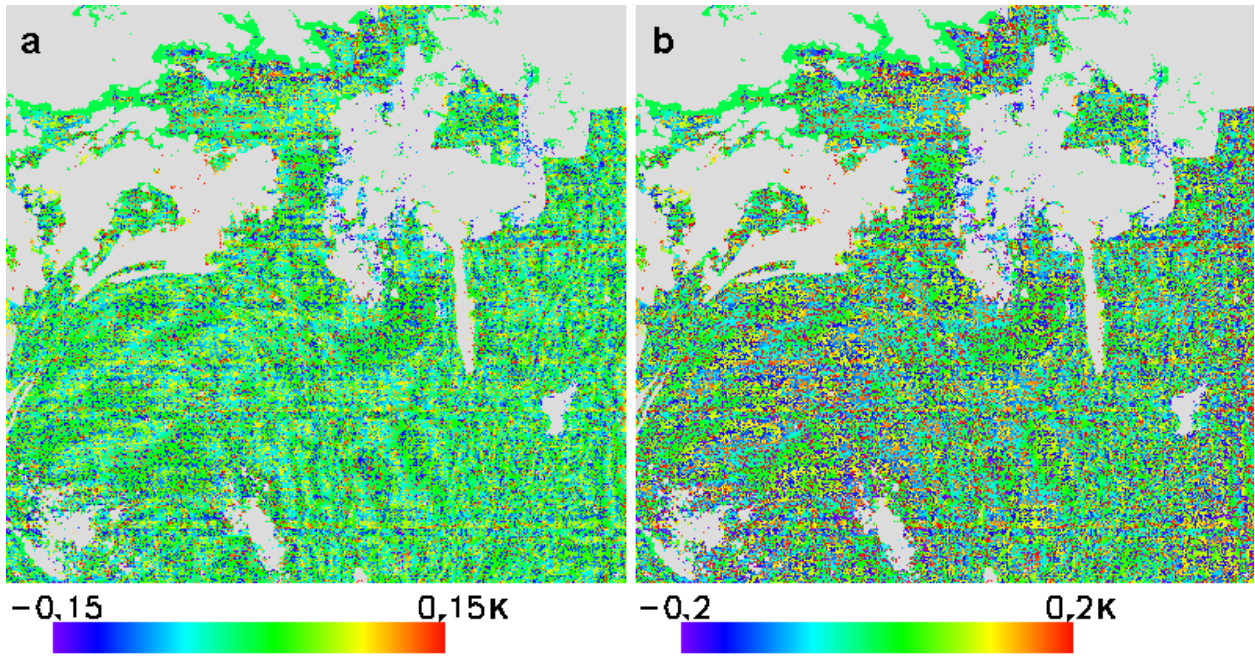


Fig. 4. Same as in Fig.2 but with ΔT_B^* obtained from Eq. (9a-c) with 11×11 sliding window and $\sigma_{max}=0.15$ K.

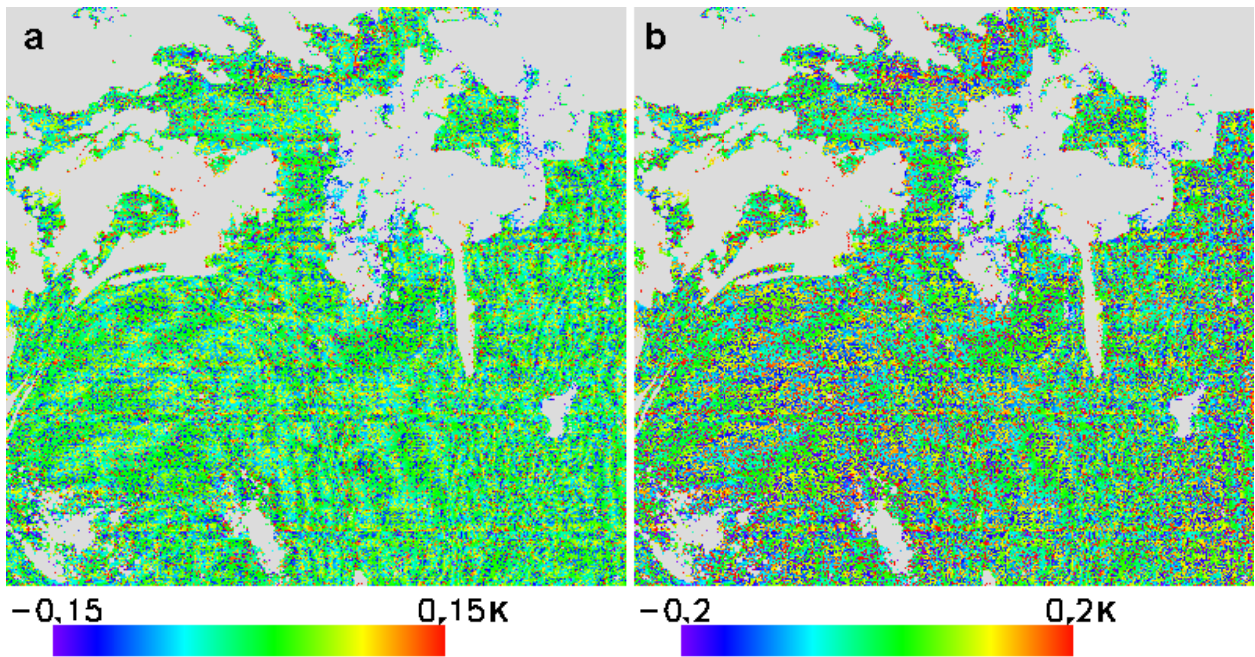


Fig. 5. Same as in Fig.2 but with ΔT_B^* obtained from Eq. (9) using an additional 3×3 sliding window.

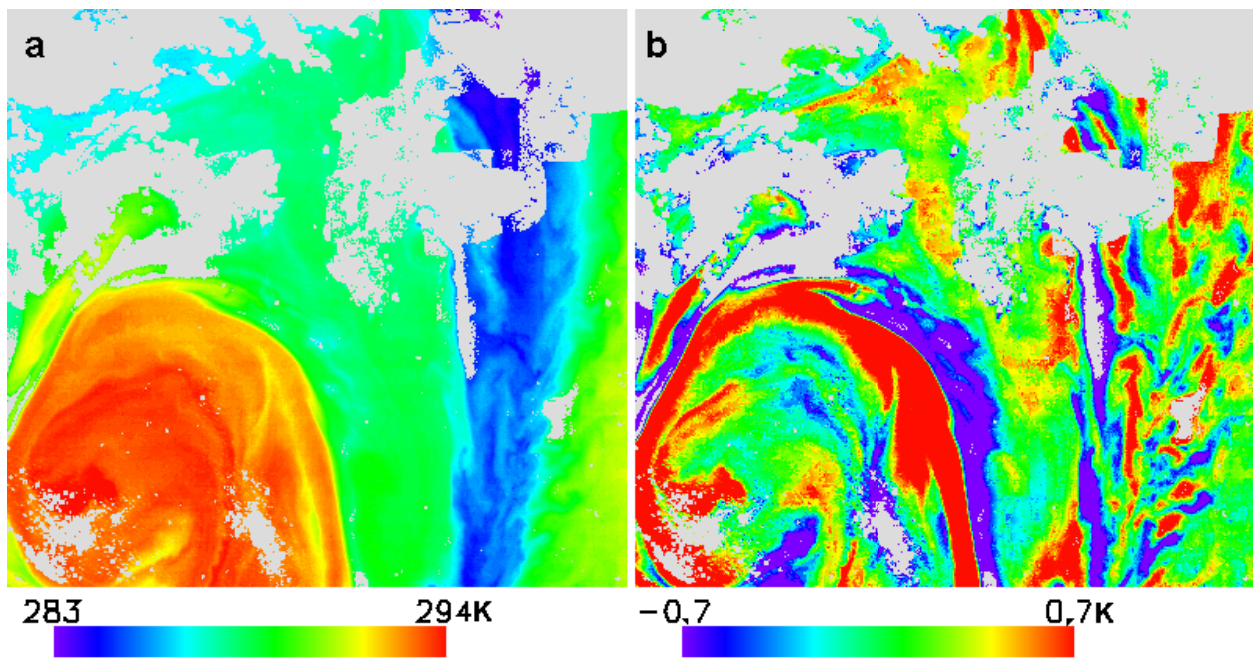


Fig.6. Same as in Fig. 1c and Fig. 1d using the final version of the ACSPO smoothing algorithm.

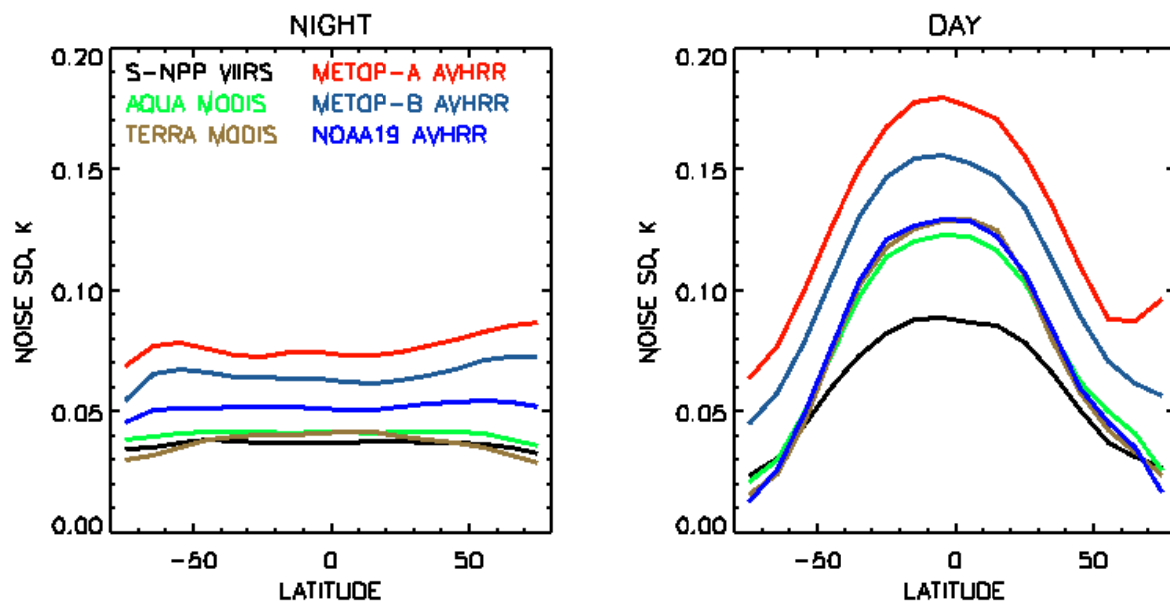


Fig. 7. RMS suppressed noise in SST as function of latitude, for six satellite sensors and for (left panel) night and (right panel) day.

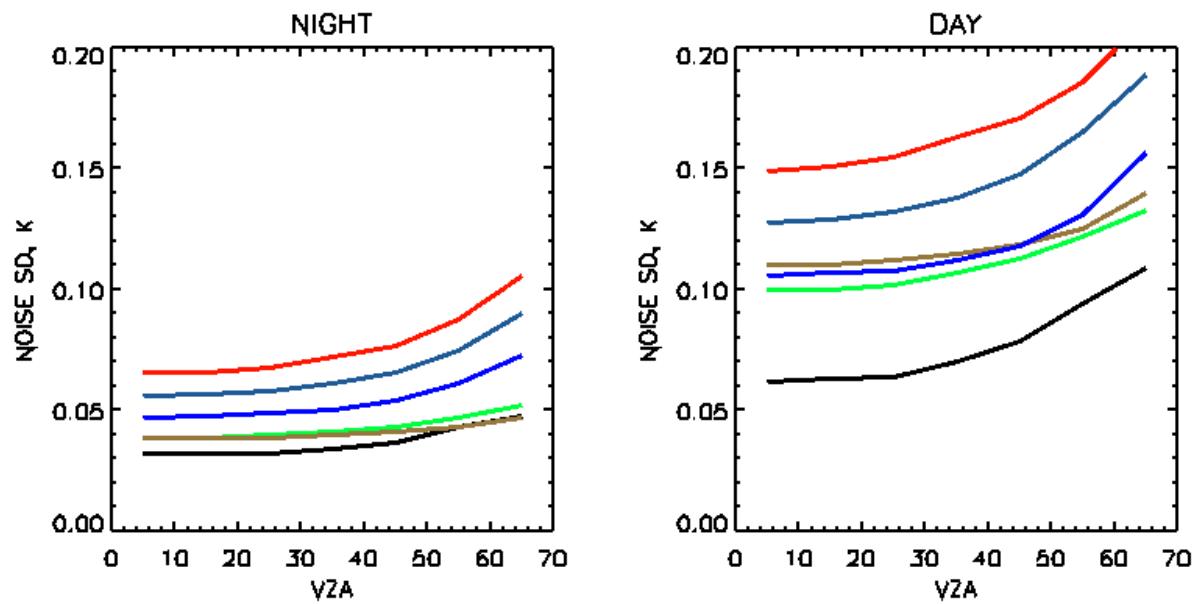


Fig. 8. RMS suppressed noise in SST as function of VZA, for six satellite sensors and for (left panel) night and (right panel) day.